ORIGINAL ARTICLE

Boosting synergism of chemo- and immuno-therapies *via* switching paclitaxel-induced apoptosis to mevalonate metabolism-triggered ferroptosis by bisphosphonate coordination lipid nanogranules

Ge Song[a,b,†], Minghui Li[a,b,†], Shumin Fan[a,b,†], Mengmeng Qin[a,b], Bin Shao[c], Wenbing Dai[a,b], Hua Zhang[a,b], Xueqing Wang[a,b], Bing He[a,b,*], Qiang Zhang[a,b,*]

[a]*Beijing Key Laboratory of Molecular Pharmaceutics and New Drug Delivery Systems, School of Pharmaceutical Sciences, Peking University, Beijing 100191, China*
[b]*State Key Laboratory of Natural and Biomimetic Drugs, School of Pharmaceutical Sciences, Peking University, Beijing 100191, China*
[c]*Department of Medical Oncology, Key Laboratory of Carcinogenesis and Translational Research (Ministry of Education), Peking University Cancer Hospital, Beijing 100142, China*

Abstract Conventional chemotherapy based on cytotoxic drugs is facing tough challenges recently following the advances of monoclonal antibodies and molecularly targeted drugs. It is critical to inspire new potential to remodel the value of this classical therapeutic strategy. Here, we fabricate bisphosphonate coordination lipid nanogranules (BC-LNPs) and load paclitaxel (PTX) to boost the chemo- and immuno-therapeutic synergism of cytotoxic drugs. Alendronate in BC-LNPs@PTX, a bisphosphonate to block mevalonate metabolism, works as both the structure and drug constituent in nanogranules, where alendronate coordinated with calcium ions to form the particle core. The synergy of alendronate enhances the efficacy of paclitaxel, suppresses tumor metastasis, and alters the cytotoxic mechanism. Differing from the paclitaxel-induced apoptosis, the involvement of alendronate inhibits the mevalonate metabolism, changes the mitochondrial morphology, disturbs the redox homeostasis, and causes the

*Corresponding authors.
E-mail addresses: hebingmumu@bjmu.edu.cn (Bing He), zqdodo@bjmu.edu.cn (Qiang Zhang).
†These authors make equal contributions to this work.

accumulation of mitochondrial ROS and lethal lipid peroxides (LPO). These factors finally trigger the ferroptosis of tumor cells, an immunogenic cell death mode, which remodels the suppressive tumor immune microenvironment and synergizes with immunotherapy. Therefore, by switching paclitaxel-induced apoptosis to mevalonate metabolism-triggered ferroptosis, BC-LNPs@PTX provides new insight into the development of cytotoxic drugs and highlights the potential of metabolism regulation in cancer therapy.

1. Introduction

Conventional chemotherapy based on cytotoxic drugs is the most common and widely accepted therapeutic strategy for patients with advanced carcinoma[1]. These cytotoxic drugs kill cancer cells by disrupting essential cellular processes associated with cell proliferation and anabolic metabolism, including inducing DNA fragmentation, inhibiting cytoskeleton activity, and blocking ATP synthesis[2]. Because of their broad validity against multiple carcinomas, most cytotoxic drugs are incorporated in the first-line treatment regimen[3,4], and some have been used in clinics for over 30 years. Nevertheless, many patients frequently suffer from the side effects of cytotoxic drugs due to their low selectivity and non-specificity in tumor therapy[5]. Additionally, their long-term administration may lead to drug resistance, which attenuates the therapeutic effects[6]. Following the incremental application of monoclonal antibodies and molecularly targeted drugs, the development of new cytotoxic drugs is confronted with serious challenges in recent years[7]. Therefore, it is becoming a key issue to inspire new potential to remodel the value of this classical therapeutic strategy.

Previous studies have reported that several cytotoxic drugs kill cancer cells via a special mechanism termed immunogenic cell death (ICD)[8], instead of the classical apoptosis mechanism. ICD is a programmed cell death mode, in which dying cancer cells release high levels of damage-associated molecular patterns (DAMPs) after exposure to cytotoxic drugs[9]. These endogenous DAMPs are recognized by antigen-presenting cells (APCs) to induce an enhanced innate immune response. The activated APCs promote T cell-mediated adaptive immunity, especially by activating cytotoxic T lymphocytes, which can directly recognize and kill cancer cells by releasing perforin and granzyme[10]. Because of the synergism between ICD and immunity, combinatorial therapy involving cytotoxic drugs and immune checkpoint blockers such as anti-programmed cell death protein 1 (PD-1), anti-programmed death ligand 1 (PD-L1), and anti-CTLA4 antibodies, has been approved by FDA for clinical use to improve the prognosis of patients[11]. Briefly, the ICD effect markedly expands the scope of cytotoxic drugs for cancer therapy[12]. However, it should be noted, apoptosis is still the primary mechanism that most cytotoxic drugs including doxorubicin and paclitaxel cause cancer cell death[13]. Compared with the necrotic cell death mode, in which the cell membrane is broken and numerous DAMPs are released, apoptosis has weak immunogenicity because the cellular components are retained in the form of apoptotic bodies during the cell death process. Apoptotic bodies are recognized and phagocytosed by macrophages without inducing an inflammatory response[14]. Therefore, to enhance the efficacy of cytotoxic drugs, converting drug-induced cell death to ICD is an effective strategy to increase the anti-tumor synergism between chemotherapy and immunotherapy. Reportedly, the immunogenicity of tumors after treatment with cytotoxic drugs is markedly increased via the introduction of multiple functional delivery materials, like inorganic polymers[15], or of different biomedical technologies, such as irradiation[16] and ultrasound[17]. These strategies enhance the sensitivity of cancer cells to cytotoxic drugs by primarily inducing necrotic cancer cell death, resulting in the release of DAMPs as immune agonists, which improves the efficacy of cytotoxic drugs[18].

Ferroptosis is a process of programmed cell death that increases cellular immunogenicity[19]. Mechanically, ferroptosis is derived from the restricted elimination and excessive accumulation of lethal lipid peroxides (LPO), which impair the membrane structure and cause the release of endogenous DAMPs[20]. Three vital regulatory mechanisms[21], including the synthesis and peroxidation of polyunsaturated fatty acid (PUFA)-containing polyunsaturated-fatty-acid-containing phospholipids (PUFA-PLs)[22], iron metabolism[23], and mitochondrial metabolism[24], have been demonstrated to control LPO homeostasis. The disruption of any regulatory pathway may lead to ferroptosis. Multiple regulatory factors of these pathways have been verified to sensitize cancer cells to immunotherapy. For instance, in combination with a GPX4 inhibitor, the sensitivity of cancer cells and xenograft tumors to the chemotherapeutic agent gemcitabine was increased by inducing ferroptosis, and elastin-loaded nanoreactors induced ferroptosis by impacting the GPX4/GSH pathway, thereby improving the treatment of triple-negative breast cancer[25]. However, notably, most ferroptosis-based synergistic delivery strategies are devoted to disrupting the production of PUFA-PLs by disturbing the activity of relevant metabolic enzymes or directly changing the iron metabolism using Fenton's reaction[21]. The capacity and function of mitochondrial metabolism to synergize with cytotoxic drugs via the regulation of ferroptosis have not been elucidated.

Ubiquinone, also known as coenzyme Q (CoQ), is a vital regulator of ferroptosis, which is based on mitochondrial metabolism. It controls electron transfer from the respiratory chain complex I or II to complex III in the mitochondria, enabling the production of ATP[26]. Ubiquinone (CoQ) is interconverted with its reduced form ubiquinol (CoQH$_2$). CoQ-CoQH$_2$ equilibrium regulates and maintains redox homeostasis in the mitochondria[27]. However, once the homeostasis is disrupted, CoQ causes the generation of reactive oxygen species (ROS) in mitochondria and facilitates the ROS-induced accumulation of LPO, leading to ferroptosis[28]. Therefore, disturbing the CoQ-CoQH$_2$ equilibrium is key for mitochondrial metabolism-based ferroptosis. Moreover, CoQ is closely regulated by the mevalonate metabolism pathway, where CoQ is catalyzed to conjugate with a geranylgeranyl moiety by geranylgeranyltransferase, using geranylgeranyl diphosphate

(GGPP) as the substrate[29]. Because only geranylgeranyl CoQ can accurately anchor in the mitochondrial membrane to control electron transfer, mevalonate metabolism becomes a vital upstream signal for the maintenance of CoQ-CoQH$_2$ equilibrium and ferroptosis. Mevalonate metabolism is fueled by acetyl-CoA, NADPH, and ATP to synthesize cholesterol and prenylated proteins[30]. Since multiple carcinomas exhibit enhanced lipid metabolism, blocking the mevalonate pathway using statins suppresses tumor proliferation[31]. Nevertheless, the role of the mevalonate pathway in regulating mitochondrial metabolism-based ferroptosis is unclear. Moreover, it is unclear whether the inhibition of the mevalonate pathway sensitizes cancer cells to the immune system and combines with cytotoxic drugs to enhance the synergistic efficacy of chemotherapy and immunotherapy.

In the present study, we selected alendronate, an inhibitor of farnesyl diphosphate synthase (FDPS) in the mevalonate pathway, to block the synthesis of farnesyl diphosphate (FPP) and GGPP, to restrain the prenylation of CoQ and induce the subsequent turbulence of redox homeostasis in mitochondria. A classical cytotoxic drug paclitaxel was combined with the metabolic regulator alendronate in this study. To achieve co-delivery of both paclitaxel and alendronate to target tumor tissue, we designed and fabricated paclitaxel-loaded bisphosphonate coordination lipid nanogranules (BC-LNPs@PTX) (Fig. 1). BC-LNPs@PTX had a "core−shell" structure, where alendronate coordinated with calcium ions to constitute the solid core, and a lipid layer containing paclitaxel was coated to form the shell. Moreover, we characterized the nanogranules and investigated their intracellular behavior and cytotoxic effects. In particular, the synergistic cytotoxicity exerted by the nanoparticulated alendronate in BC-LNPs@PTX was evaluated. Proteomics, metabolomics, and mitochondrial metabolism analyses were performed to explore the cell death mechanism induced by BC-LNPs@PTX. Additionally, the effect of BC-LNPs@PTX on the migration and invasion of cancer cells was investigated. Finally, multiple tumor-bearing mouse models were constructed to verify the *in vivo* efficacy of BC-LNPs@PTX against tumor proliferation and metastasis and to assess the sensitivity of BC-LNPs@PTX to immunotherapy.

2. Materials and methods

2.1. Preparation and characterization of BC-LNPs@PTX

BC-LNPs were prepared using the reverse microemulsion method[32,33]. We added (drop-wise) 0.1 mL of aqueous 0.5 mol/L calcium chloride salt (CaCl$_2$) solution to 8 mL of oil phase mixture composed of 0.6 mol/L Triton X-100/1.5 mol/L 1-hexanol in cyclohexane and stirred the mixture at 25 °C for 30 min at 600 rpm. Next, we prepared a microemulsion using 0.1 mL of 0.05 mol/L alendronate sodium salt solution as described above and added 0.32 mL of dioleoyl-*sn*-glycero-3-phosphate sodium salt (DOPA, 20 mmol/L in CHCl$_3$) to the prepared microemulsion. Subsequently, the bisphosphonate microemulsion was added to the CaCl$_2$ microemulsion at a flow rate of 0.2 mL/min. The obtained microemulsion mixture was continuously stirred for 30 min at 600 rpm, 32 mL of ethanol was added, and centrifuged at 10,000 rpm for 10 min to obtain the DOPA-doped core of the BC-LNPs. Finally, after washing once with ethanol and twice with

50% (*v/v*) ethanol/chloroform, the precipitate was re-dispersed in 200 μL of chloroform.

Lipid-coated nanogranules were synthesized *via* the filming hydration method. We dissolved 1.6 mg of DOPC and 2.0 mg of DSPE-PEG2000 with DOPA-doped cores in chloroform. The solvent was removed by rotary evaporation, and the film was subsequently hydrated in phosphate-buffered saline (PBS) solution (maintained at 60 °C) by vortexing. For BC-LNPs@PTX, 0.9 μg of paclitaxel was dissolved in the chloroform before filming.

The hydrodynamic diameter of the BC-LNPs in water was evaluated by dynamic light scattering (DLS) analysis using a Malvern Zetasizer Nano ZS (Malvern, UK). Transmission electron microscopy (TEM) (JEOL, Japan) was performed to observe the morphology of the BC-LNPs. The crystalline structure of the nanogranules was confirmed using X-Ray Powder Diffraction (XRD) on a MiniFlex diffractometer (Rigaku, Japan). Furthermore, to elucidate the distribution of elements in non-DOPA-coated cores we performed energy-dispersive X-ray spectroscopy (EDX) with high-resolution transmission electron microscopy (HRTEM) (JEOL, Japan) using an EDX detector system.

2.2. Apoptosis assay and cell cycle analysis

For apoptosis assay, 4T1 cells were seeded in 6-well plates (3 × 10^5 cells/well) and incubated overnight at 37 °C. After incubation with comparable concentrations of free paclitaxel, BC-LNPs, and BC-LNPs@PTX for 12 h, the cells from each group were digested using trypsin without EDTA and centrifuged at 170 × *g* for 3 min. Untreated cells were used as controls. Next, anti-annexin-V-FITC and propidium iodide were added to the samples, and the samples were incubated for 20 min in the dark. The cells were immediately analyzed using a flow cytometer (FCM, BD, USA).

For cell cycle analysis, 4T1 cells were seeded in 6-well plates (3 × 10^5 cells/well) and incubated overnight at 37 °C. They were divided into groups treated with comparable concentrations of free paclitaxel, BC-LNPs, or BC-LNPs @PTX. After 12 h, the medium was removed, and the cells were digested using trypsin and harvested by centrifugation at 170× *g* for 3 min. The harvested cells were fixed in 70% ethanol at 4 °C for 12 h. After staining with propidium iodide, the samples were analyzed using FCM.

2.3. Proteomics-based evaluation of antitumor efficacy of BC-LNPs@PTX

The potential mechanism of BC-LNPs was determined using proteomics by splitting proteins into experimental cells. Proteins were isolated using sodium dodecyl sulfate-polyacrylamide gel electrophoresis, then digested and the obtained peptides were analyzed using liquid chromatography with tandem mass spectrometry (LC−MS/MS). Briefly, the peptides were first loaded on a C18 precolumn (Thermo Fisher Scientific, USA) and then separated using nano-LC−MS/MS. LTQ Orbitrap Velos Pro or Q-Exactive HF (Thermo Fisher Scientific, USA) was used for mass spectrometric analysis; a data-dependent CID model or HCD model was used for the acquisition of MS/MS data; the Perseus software was used to analyze raw data; and MS/MS data were searched against the Proteome Discoverer, Universal Protein Database, and PANTHER databases.
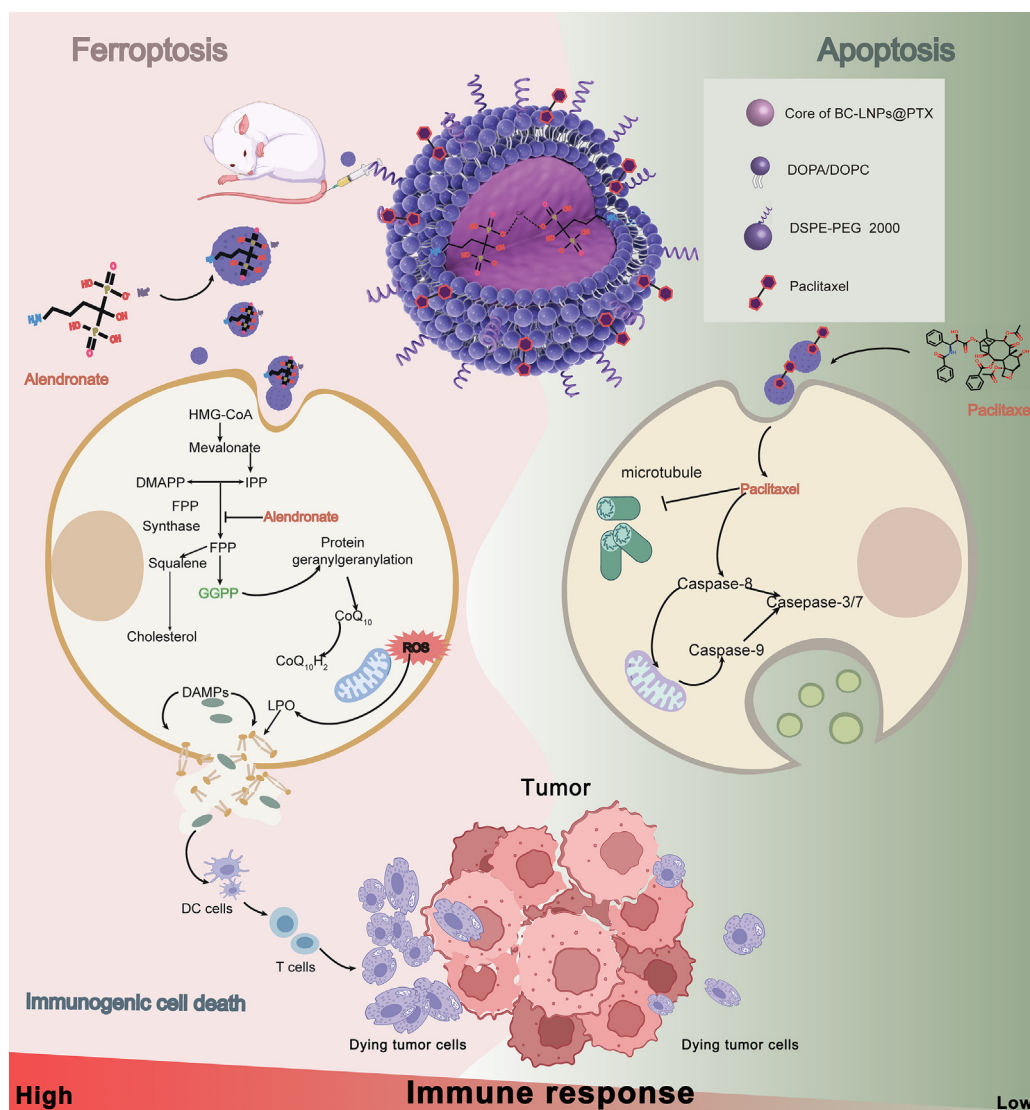
Figure 1 Schematic diagram of BC-LNPs@PTX switching apoptosis to ferroptosis to achieve synergism of chemo- and immune-therapies of tumors. In brief, in this study, the classical cytotoxic drug paclitaxel was combined with the metabolic regulator alendronate by fabricating paclitaxel-loaded bisphosphonate coordination lipid nanogranules (BC-LNPs@PTX) to achieve the co-delivery of both paclitaxel and alendronate targeting to the tumor tissue. BC-LNPs@PTX had a "core−shell" structure, where alendronate coordinated with calcium ions to constitute the solid core, and a lipid layer containing paclitaxel was coated to form the shell. Differing from the paclitaxel-induced apoptosis, the involvement of nanoparticulated alendronate changed the mitochondrial morphology and metabolism, disturbed the redox homeostasis, and caused the accumulation of mitochondrial ROS and lethal lipid peroxides (LPO). These factors finally triggered the ferroptosis of tumor cells. As a process of immunogenic cell death (ICD), the ferroptosis caused by BC-LNPs@PTX remodeled the suppressive tumor immune microenvironment and effectively synergized with the immunotherapy.

2.4. Untargeted metabolomics for the identification of metabolic regulatory mechanisms of BC-LNPs@PTX

The changes in the biological metabolic activities in the 4T1 cells during the treatment process were analyzed using the untargeted metabolomics approach. After immersion in liquid nitrogen, the 4T1 cellular samples were ground adequately, followed by UPLC−MS/MS analysis. The extracted metabolites were loaded on a C18 column (Waters, USA) and separated using UPLC (Waters, USA), and high-resolution MSE mass spectrometry was performed on a Vion IMS QTof (Waters, USA). The spectrometry data were imported into the Progenesis QI 2.3 software and searched against the METLIN database (a metabolite and chemical entity database), Kyoto Encyclopedia of Genes and Genomes (KEGG), and Human Metabolome Database (HMDB).

2.5. Regulation of mitochondrial function by BC-LNPs

The intracellular energy metabolic characteristics were determined using mitochondria-related analysis. 4T1 cells were seeded in 12-well plates (1×10^5 cells/well) and incubated overnight at 37 °C. After individually incubating 4T1 cells with comparable concentrations of free paclitaxel, BC-LNPs and BC-LNPs@PTX for 18 h, the cells were treated with 2-(N-(7-nitrobenz-2-oxa-

1,3-diazol-4-yl) amino)-2-deoxyglucose (2-NBDG), NBD-labeled cholesterol (NBD-Chol), or 4,4-difluoro-5,7-dimethyl-4-bora-3a,4a-diaza-s-indacene-3-hexadecanoic acid (BODIPY C16) to detect glucose, cholesterol, and fatty acid related cellular uptake. Intracellular ROS and LPO levels were evaluated using a 2′,7′-dichlorodihydrofluorescein diacetate (DCFH-DA)-based ROS assay kit and BODIPY C11, respectively. The fluorescence signals from 2′,7′-dichlorofluorescein (DCF), induced by the presence of ROS and BODIPY C11 and promoted by the accumulation of LPO, were quantified using FCM. ROS specifically generated by mitochondria were isolated *via* blockage of the NADPH pathway by apocynin. LPO production was suppressed by GGPP, a downstream metabolite of the mevalonate pathway, and mitochondrial morphology was observed using a confocal laser scanning microscope (Leica, Germany) after JC-1 staining. Mitochondrial membrane homeostasis is characterized by its membrane potential ($\Delta\Psi_m$), which is reflected by JC-1 staining, the production of JC-1 monomer indicating the loss of membrane potential.

2.6. Migration and invasion assay of tumor cells

4T1 cells (3×10^4 cells/well) were seeded in 100 μL of complete medium in the apical chamber of a 24-well 8-μm transwell polycarbonate membrane with or without extracellular matrix (ECM) for 12 h for adherence, and 600 μL of complete medium was added to the basolateral chamber. Then, the apical chamber was replaced with a blank medium with or without BC-LNPs/BC-LNPs@PTX, and the basolateral side was replaced with a blank/complete medium for another 12 h. Apical and basolateral chambers with the blank medium were set as a negative control, and nutrition gradient without drugs was set as a positive control, respectively. The nutrition gradient was supplied to other groups containing different formulations, with or without GGPP. Residual cells on the upper side of the membrane were stained with crystal violet and quantified using an XDS-1B inverted biological microscope (COIC, China). The relative migration rate was calculated as Eq. (1):

$$\text{Relative migration (\%)} = \text{Number of cells in the experimental group/Number of cells in the negative control group} \times 100 \qquad (1)$$

High-content analysis was also performed using 4T1 cells. Briefly, we seeded 4T1 cells (5×10^3/well) in a 96-well plate and incubated the plate for 12 h for adherence. Next, comparable concentrations of free paclitaxel, BC-LNPs, and BC-LNPs@PTX, or complete medium were added to the cells, and the cells were incubated for 12 h. We captured images every 20 min for 12 h using an Operetta High-Content Analysis System (PerkinElmer, USA) equipped with a 20 × objective and a bright-field & digital phase contrast (DPC) dual channel. Then, cell trajectory tracking and movement parameters (square displacement, track straightness, speed, and distance) were performed and calculated, respectively, using Software Harmony 3.5.1.

2.7. Analysis of anti-tumor efficacy of BC-LNPs@PTX in vivo

The 4T1 subcutaneous tumor model was established by subcutaneous inoculation of 3×10^5 4T1 cells into the right hind leg of female BALB/c mice. Five days post-inoculation, the mice were randomly divided into five groups. Subsequently, saline, Taxol, PC-LNPs, BC-LNPs, or BC-LNPs@PTX were administered to the tumor model mice of each group *via* tail vein injection once every other day (five times in total). The administered dose of alendronate and paclitaxel was 13.5 and 10 mg/kg, respectively. The tumor volume and body weight of each group were recorded every alternate day. Tumor volume was calculated using Eq. (2):

$$V = 1/2 \times a \times b^2 \qquad (2)$$

where *a* and *b* represent the length and width of the tumor, respectively, which was measured using a digital caliper.

On the day after the last injection, whole blood samples from each group were collected and diluted for hematology analysis; the red blood cell (RBC), white blood cell (WBC), platelet, granulocyte (GR), and lymphocyte (LY) counts were evaluated using a HITACHI7020 automatic biochemical analyzer (HITACHI, Japan).

The 4T1 orthotopic tumor model was established by inoculation of 3×10^5 4T1 cells into the fat pad of the fourth pair of mammary glands on the right side of female BALB/c mice. The other procedures were consistent with the subcutaneous tumor model.

For the determination of tumor-infiltrating T lymphocytes, the 4T1 tumor model was established by subcutaneous inoculation of 3×10^5 4T1 cells in the alar of BALB/c mice. When the tumor volumes reached about 200 mm³ (Day 0), the mice were randomly divided into four groups. Saline, Taxol, BC-LNPs, and BC-LNPs@PTX were respectively given to the tumor model mice every other day *via* tail vein injections, 4 times in total. On Day 7, the mice were sacrificed, and serum, spleens, and tumors were collected and digested at 37 °C for 40 min in the presence of collagenase, hyaluronidase, and DNase. After filtration through a 70 μm screen, immune cells were isolated with leukocyte separation solution, then counted and diluted to 1×10^7/mL. The samples were stained with the anti-mouse CD3 APC, anti-mouse CD4 PE/Cy7, anti-mouse CD8α AF488, and anti-mouse CD25 PE to detect CD4 T, CD8 T, and Treg cells. To detect the activation of DCs in tumor-draining lymph nodes (TDLNs), TDLNs from each group of mice were collected and prepared to single-cell suspensions. The samples were stained with anti-mouse CD11c PE/Cy7, anti-mouse CD80 PE, and anti-mouse CD86 FITC to detect the maturation of DCs.

To evaluate the synergistic effect of immunotherapy with PD-L1 antibodies, a 4T1 tumor model was established subcutaneously, as described previously. The mice were randomly divided into six groups: saline, Taxol, BC-LNPs, BC-LNPs@PTX, BC-LNPs@PTX + anti-PD-L1 (αPD-L1), and αPD-L1. αPD-L1 (100 μg) was intraperitoneally injected on Days 6, 10, and 14. Other preparations were administered through the tail vein every other day, starting on Day 5 (a total of six injections). The body weight and tumor volumes of the mice were measured on alternate days, and growth curves of the tumor volumes were drawn. On

Day 17, the mice were sacrificed, and their tumors and lungs were isolated. The tumors were weighed and photographed, and the lung metastases were observed and counted.

2.8. Analysis of anti-metastasis efficacy of BC-LNPs@PTX in vivo

Firstly, we constructed a lung metastasis model from chronic subcutaneous 4T1 tumors The 4T1 tumor model was established, and the administration regimen as described previously. BALB/c mice were divided and treated as described in the previous section. On Day 21, the mice were sacrificed, and the major organs, including the heart, liver, spleen, kidney, and lung, were harvested from each group. The organs were fixed using a 4% paraformaldehyde solution, followed by hematoxylin and eosin (H&E) staining to observe the pathology of major tissue sections to evaluate the safety of the BC-LNPs. Whole blood samples (1 mL) were collected from each mouse and centrifuged at 8000 rpm for 15 min to obtain serum. Liver and renal functions of the experimental animals were evaluated by measuring the levels of aminotransferase (ALT), aspartate aminotransferase (AST), alkaline phosphatase (ALP), and uric acid (UA) in the serum samples. Moreover, the lung tissue samples from each group were stained using Bouin's fluid to detect metastatic nodules and examined.

In addition, we established a short-term lung metastasis by tail vein injection of 4T1 cells using female BALB/c mice. To determine the metastatic locus, 4T1 cells stably transfected with luciferase (4T1-luc cells) were used. Animals were randomly divided into five groups and injected with 1×10^5 4T1-luc cells via the tail vein to induce lung metastasis. At 12 h post-inoculation, saline, Taxol, PC-LNPs, BC-LNPs, or BC-LNPs@PTX were administered to the mice of each group once every other day (five times) via tail vein injections. On Day 13, the mice were intraperitoneally injected D-luciferin potassium salt solution. Bioluminescence signals were recorded 15 min post-injection using an IVIS (Perkin−Elmer, USA).

To study the induction of immune memory in vivo, the 4T1 tumor model and administration strategy were the same as described in the determination of tumor-infiltrating T lymphocytes. Spleens were cut, ground, and sieved to prepare single-cell suspensions. After centrifugation, 1 mL red blood cell lysate was added and lysed for 5 min on ice to shatter red blood cells. After washing twice, count and dilute to 1×10^7/mL. The samples were stained with the anti-mouse CD3 APC, anti-mouse CD4 PE/Cy7, anti-mouse CD8α AF488, and anti-mouse CD25 PE to detect CD4 T, CD8 T, and Treg cells. To verify the induction of pro-inflammatory cytokines, we examined the secretion of TNF-α and IL-1β in the serum of different treatment groups. The sera collected in the above experiments were assayed using TNF-α and IL-1β ELISA kits according to the instructions.

2.9. Statistical analysis

All the experiments were repeated at least three times, and all values were expressed as mean $\pm$ SEM (standard error of the mean), unless otherwise indicated. Statistical analysis was performed with the two-tailed Student's t-test. In all cases, P-value <0.05 was considered as the statistically significant difference between the two groups ($^*P < 0.05$, $^{**}P < 0.01$, $^{***}P < 0.001$, $^{****}P < 0.0001$).

3. Results and discussion

3.1. BC-LNPs@PTX enter tumor cells through the endocytosis pathway and deconstruct inside the cells in a pH-dependent manner

To increase the targeted delivery of both alendronate and paclitaxel to the tumor, we prepared BC-LNPs and loaded them with paclitaxel (BC-LNPs@PTX). BC-LNPs@PTX was composed of a solid core based on the coordination of alendronate with calcium ions and a lipid layer containing paclitaxel (Fig. 2A). DLS analysis (Fig. 2B) revealed that the average diameter of the naked bisphosphonate coordination core was 53.65 nm. Lipid coating and paclitaxel loading moderately increased the hydrodynamic diameter to 79.78 and 108.44 nm, respectively; TEM imaging (Fig. 2C) revealed the same particle size characteristics. Moreover, EDX revealed that calcium and phosphorus were homogeneously distributed throughout the structure of the nanogranules. This demonstrates the coordinated interaction between alendronate and calcium ions. XRD analysis further revealed that calcium alendronate coordination was present in the nanogranules in an amorphous form (Supporting Information Fig. S1). The zeta potential of BC-LNPs was −31.3 ± 1.04 mV, with a negative charge feature. According to two different drug extraction methods (Supporting Information Fig. S2 and Table S1), the drug loading efficiencies of BC-LNPs@PTX for alendronate and paclitaxel were determined as 40.24 ± 0.72% and 52.09 ± 0.02%, respectively. Interestingly, the loading of paclitaxel slightly increased the surface charge, which might be attributed to the altered lipid distribution owing to the embedding of paclitaxel in the lipid layer (Supporting Information Fig. S3). The mineral salt structure of the core of nanogranules is usually susceptible to acidic environments. As shown in Fig. 2D, the BC-LNPs@PTX were gradually deconstructed into smaller particles when the pH of the medium was reduced to 5.0. Particle counting using DLS technology also elucidated that the acidic environment led to the deconstruction of the nanogranules and significantly increased the number of nanogranules (Supporting Information Fig. S4). Likewise, more drugs were released from nanogranules with the deconstruction in an acidic environment (Supporting Information Fig. S5). It guaranteed the loaded drugs could effectively release into the cytoplasm and take effect once the nanogranules were delivered to tumor tissue and endocytosed by cancer cells.

Next, the cellular uptake behavior of BC-LNPs was investigated using the breast carcinoma cell line 4T1. FCM elucidated that more BC-LNPs were internalized by 4T1 cells with the increase in nanogranule concentration and incubation time (Fig. 2E and F). The internalization mechanism was investigated using the pharmacological inhibition strategy, which revealed that BC-LNPs were endocytosed by 4T1 cells through both the clathrin-mediated and caveolae-dependent pathways (Fig. 2G). As shown in Fig. 2H, the endocytosed BC-LNPs were taken into the early endosomes near the cell membrane (red border) and delivered to the late endosomes located in the perinuclear region (blue border). To elucidate the dynamics of vesicular transportation of nanogranules, the solid core and lipid layer of BC-LNPs were labeled with the fluorescent probes Ce6 and NBD-PE, respectively. The fluorescence signal of the lipid layer increased with time, suggesting that more BC-LNPs were endocytosed and located in lysosomes (Fig. 2I, K and Supporting Information Fig. S6A). In contrast, the fluorescence intensity of the core of BC-LNPs in lysosomes was reduced over time (Fig. 2J, L and Supporting
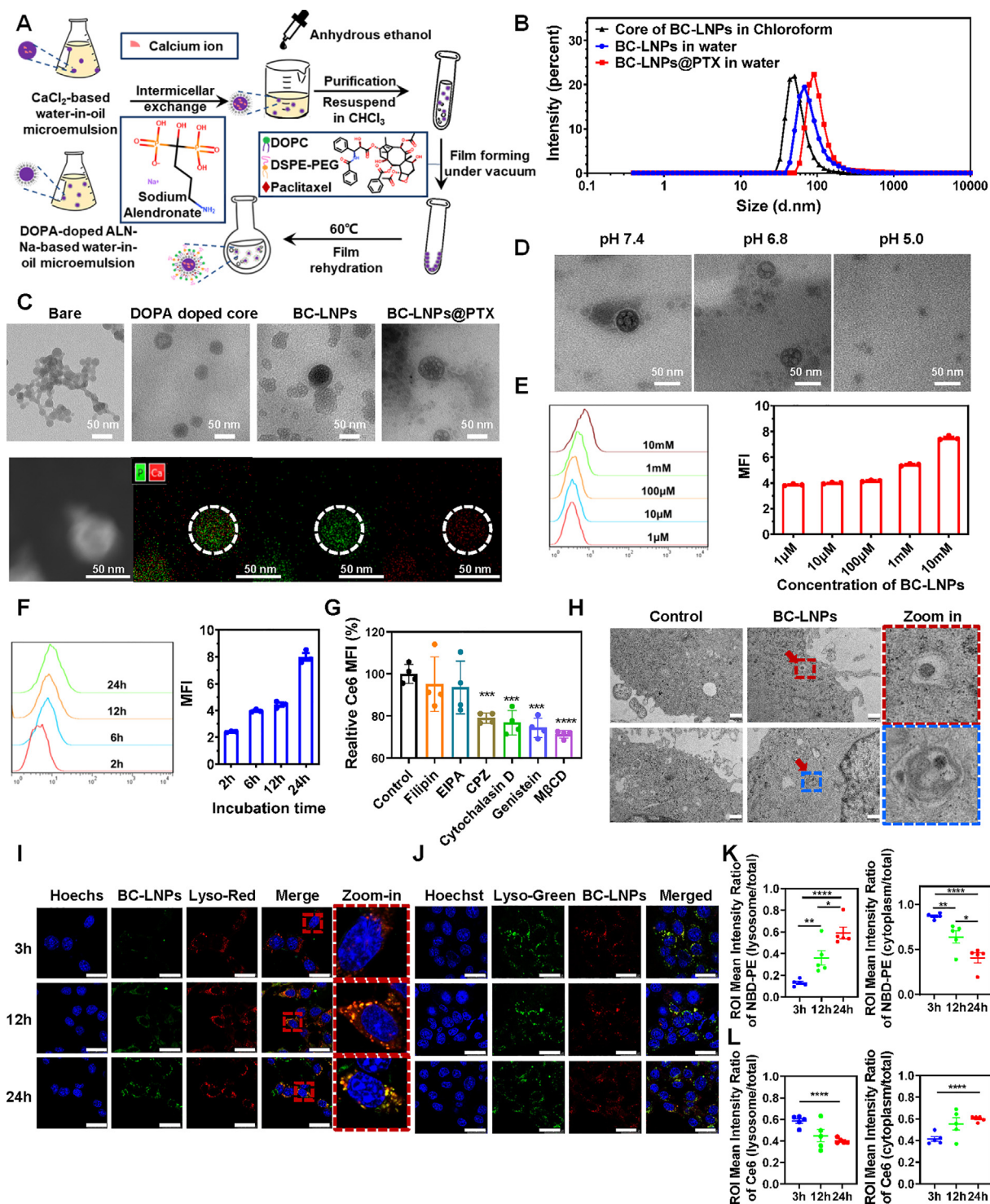
Figure 2 BC-LNPs@PTX enters tumor cells through the endocytosis pathway and deconstructs in cells in a pH-sensitive way. (A) Schematic diagram of the preparation process of BC-LNPs. (B) The particle size distributions of the core, BC-LNPs, and BC-LNPs@PTX were measured by DLS. (C) The representative TEM and EDS images of the core, BC-LNPs and BC-LNPs@PTX. Red color represented the calcium element and green color represented the phosphorus element. Bar: 50 nm. (D) Representative TEM images of BC-LNPs@PTX in buffer mediums with different pH values. Bar: 50 nm. (E) Concentration-dependent uptake of BC-LNPs detected by flow cytometry (FCM) after the incubation of 12 h, $n = 3$. MFI: mean fluorescence intensity. (F) Time-dependent uptake of BC-LNPs detected by FCM after the nanogranule incubation of 200 μg/mL, $n = 3$. (G) Cellular uptake difference of BC-LNPs at a concentration of 200 μg/mL after the treatment with different endocytosis inhibitors for 24 h, $n = 4$. (H) Representative TEM images of intracellular distribution of BC-LNPs (200 μg/mL) after the incubation of 12 h. Bar: 500 nm. (I, J) Representative CLSM images of BC-LNPs colocalized with lysosomes incubated for different time points at a concentration of
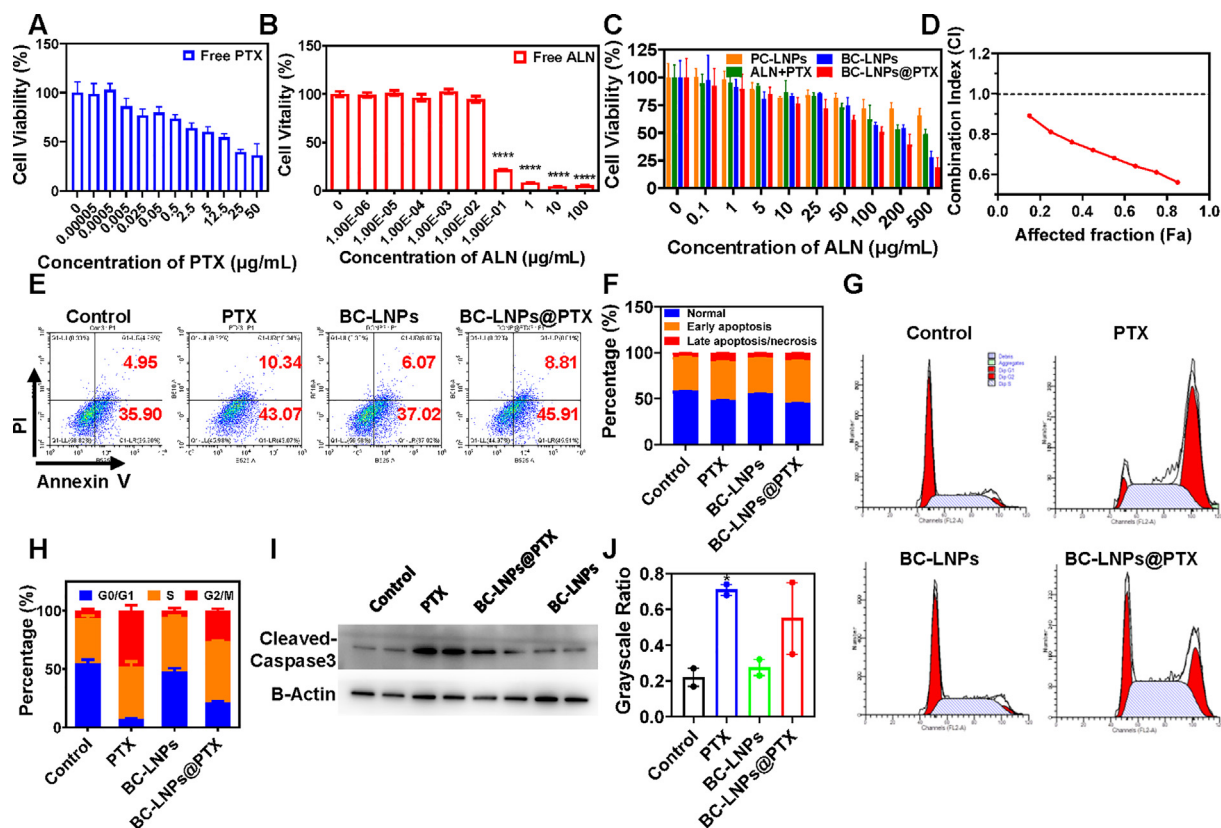
Figure 3 BC-LNPs@PTX induces tumor cell death through the synergy of alendronate with paclitaxel. (A, B) The cell viability of 4T1 cells after the incubation of free paclitaxel (A) and alendronate (B) with different concentrations. $n = 5$. (C) The cell viability of 4T1 cells after the incubation with free ALN + PTX (the ratio of ALN and PTX were consistent with those in the formulation), PC-LNPs, BC-LNPs, and BC-LNPs@PTX based on different concentrations of nanoparticulated alendronate, compared with PC-LNPs group at the same molar concentration. $n = 5$. (D) Combination index measurement of paclitaxel and nanoparticulated alendronate in BC-LNPs@PTX after the incubation of 24 h with different dose fractions (E, F) Apoptosis detection of 4T1 cells induced by PTX, BC-LNPs, and BC-LNPs@PTX was analyzed by flow cytometry (FCM) after the incubation of 12 h $n = 3$. (G, H) Cell cycle alteration of 4T1 cells induced by PTX, BC-LNPs, and BC-LNPs@PTX analyzed by FCM after the incubation of 12 h $n = 3$. (I, J) Western blotting images (I) and the corresponding quantification (J) of cleaved-caspase 3 in 4T1 cells induced by PTX, BC-LNPs, and BC-LNPs@PTX after the incubation of 12 h $n = 2$. All statistical data are presented as a mean ± SEM. The comparison was performed with the control group. *$P < 0.05$; **$P < 0.01$; ***$P < 0.001$; ****$P < 0.0001$.

Information Fig. S6B). These differential dynamics demonstrated the pH sensitivity of BC-LNPs, wherein the solid core based on coordinate interaction was dissolved and released in the acidic environment of lysosomes. Therefore, these findings indicated that both alendronate and paclitaxel could be released upon internalization of BC-LNPs@PTX by tumor cells into lysosomes.

3.2. BC-LNPs@PTX induces tumor cell death through synergy between alendronate and paclitaxel

The combined effect of alendronate and paclitaxel in BC-LNPs@PTX was evaluated using a cellular toxicity test, we used pyrophosphate coordination lipid nanogranules (PC-LNPs) as control. Pyrophosphate is not a substrate for farnesyl pyrophosphate synthetase (FPPS); therefore, it does not affect the mevalonate pathway. Because pyrophosphate can also interact with calcium ions through coordinate interactions *via* the two tandem phosphonate groups, PC-LNPs exhibited the same structural features as BC-LNPs. Additionally, PC-LNPs and BC-LNPs had the same cellular uptake behavior (Supporting Information Fig. S7). Cytotoxicity analysis revealed that BC-LNPs@PTX exhibited the most significant tumor-killing effect (Fig. 3A−C, Supporting Information Fig. S8). BC-LNPs without paclitaxel loading could also effectively induce cell death compared with that of the PC-LNPs. Notably, alendronate in BC-LNPs@PTX displayed a greater synergistic effect with paclitaxel at <50 μg/mL. The combination index analysis between alendronate and paclitaxel in BC-LNPs@PTX elucidated the same results (Fig. 3D). These findings demonstrate that BC-LNPs@PTX induced tumor cell death through the synergy between alendronate with paclitaxel.

Next, we investigated cell death after BC-LNPs@PTX treatment. To avoid the excessive cytotoxic effect caused due to long-term incubation (≥24 h), 4T1 cells were incubated with

200 μg/mL. Bar: 25 μm. BC-LNPs were labeled by NBD-PE (green) in (I) and Ce6 (red) in (J), respectively. (K, L) Fluorescence intensity ratios of BC-LNPs labeled with NBD-PE (K) and Ce6 (L) in lysosomes and cytoplasm, $n = 5$. All statistical data are presented as a mean ± SEM. The comparison was performed with the control group. *$P < 0.05$; **$P < 0.01$; ***$P < 0.001$; ****$P < 0.0001$.
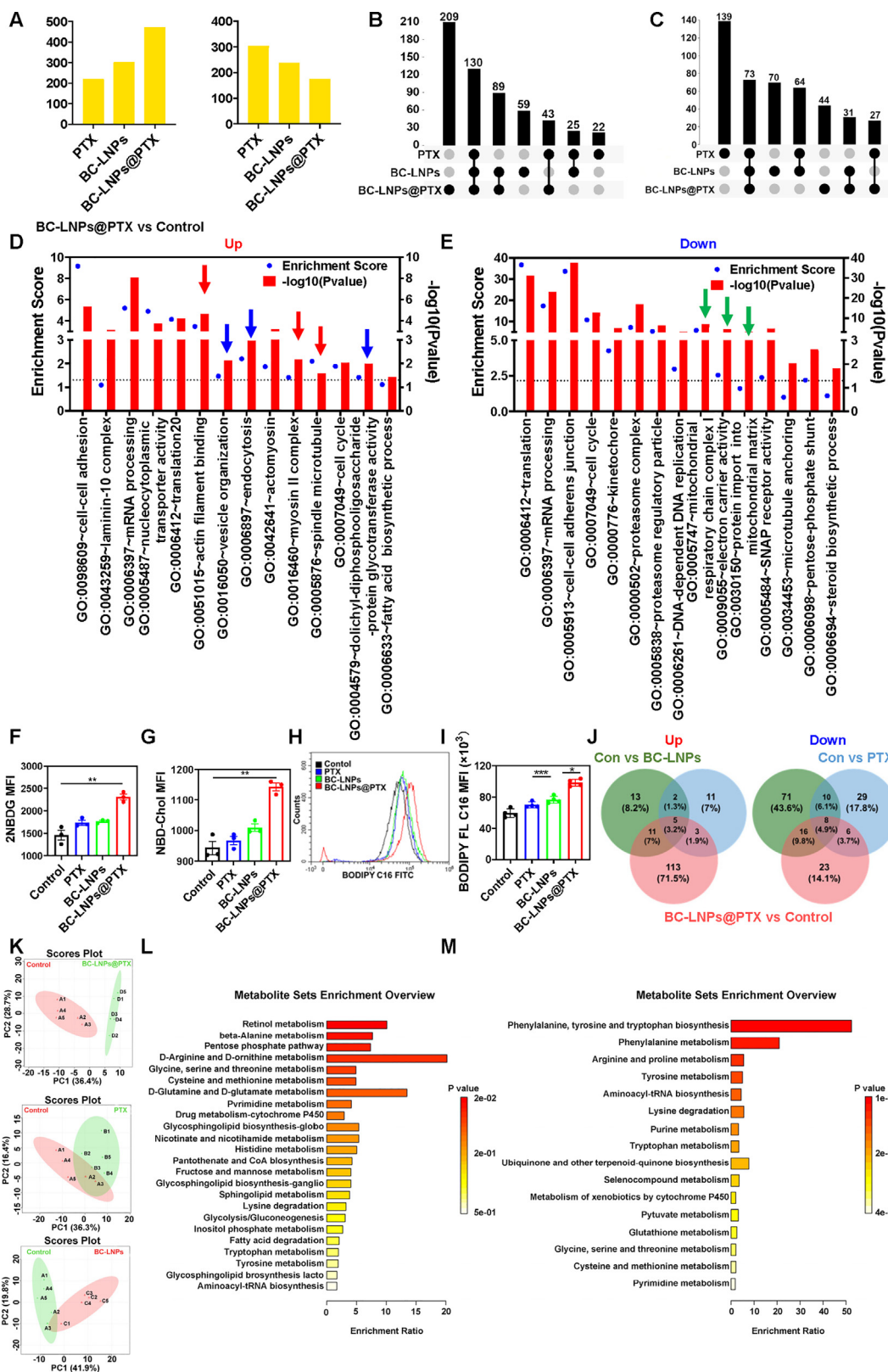
Figure 4 BC-LNPs@PTX alters the mitochondrial function and the redox homeostasis in tumor cells. (A) The number of up-regulated (left) and down-regulated (right) proteins induced by different treatments compared to the negative control detected by the label-free quantification (LFQ) based on the LC−MS/MS technology. (B, C) UpSet diagrams based on the Venn analysis of up-regulated (B) and down-regulated (C) proteins after different treatments (D, E) GO analysis of up-regulated (D) and down-regulated (E) proteins caused by BC-LNPs@PTX compared with negative control. (F) Cellular uptake of glucose analog 2-NBDG by 4T1 cells after different treatments of 18 h was detected by FCM. $n = 3$. (G) Cellular uptake of cholesterol by 4T1 cells after different treatments of 18 h was detected by FCM. $n = 3$ (H, I) Cellular uptake of fatty acid

nanogranules for 12 h in these characterization experiments. Annexin V-PI staining assay revealed that the characteristics of BC-LNPs@PTX were similar to those of the paclitaxel group, in which more apoptosis was induced than that in the control group (Fig. 3E and F). BC-LNPs without paclitaxel loading exhibited slightly increased apoptosis and necrosis of tumor cells during the 12-h incubation period. Moreover, the cell cycle assay revealed an obvious effect of BC-LNPs. As shown in Fig. 3G and H, BC-LNPs@PTX significantly changed the classical cell cycle model induced by paclitaxel. The proportion of cells that remained in the G2/M phase after incubation with BC-LNPs@PTX was reduced compared with that in the paclitaxel group. Moreover, a higher number of cells remained in the S phase due to the introduction of alendronate after BC-LNPs@PTX treatment. Western blotting revealed that the cleavage of caspase-3, the key initiator of apoptosis, was also attenuated in the BC-LNPs@PTX group compared to that in the paclitaxel group (Fig. 3I and J). These findings indicate that alendronate, as the structural constituent of the solid core of BC-LNPs, synergizes with paclitaxel to kill tumor cells through a mechanism other than apoptosis.

3.3. BC-LNPs@PTX alters mitochondrial function and redox homeostasis in tumor cells

To elucidate the underlying mechanism of the cytotoxicity exhibited by BC-LNPs@PTX, we investigated protein expression and metabolite production in 4T1 cells after incubation with nanogranules using proteomics and metabolomics. Both the BC-LNPs and free paclitaxel group were used as controls. First, the variation in protein expression caused by BC-LNPs@PTX was detected using label-free quantification (LFQ) based on the LC−MS/MS technology. Correlation analysis among replicates revealed that the coefficients were >0.75, demonstrating the feasibility of the detection method (Supporting Information Fig. S9). All obtained data were compared with that of the negative control to determine changes in protein expression. As shown in Fig. 4A, treatment with BC-LNPs@PTX, BC-LNPs, and free paclitaxel changed the protein expression profile of 4T1 cells; BC-LNPs@PTX treatment upregulated 471 proteins and downregulated 175 proteins. Similarly, 330 and 220 proteins were upregulated by BC-LNP and free paclitaxel treatments, respectively. Moreover, Venn diagram analysis revealed that fewer proteins overlapped between the BC-LNPs@PTX and free paclitaxel groups (Fig. 4B and C). In contrast, more proteins, including 89 upregulated and 64 downregulated proteins, overlapped between the BC-LNPs@PTX and BC-LNPs groups. This indicated that nanoparticulated alendronate markedly altered cellular responses to paclitaxel treatment. According to the functional annotation clustering based on the database for annotation, visualization, and integrated discovery (DAVID) bioinformatics resource (Fig. 4D and E, Supporting Information Fig. S10), BC-LNPs@PTX treatment significantly downregulated the expression of proteins associated with microtubules and actin, which were categorized as spindle microtubules (GO:0005876), actin filament binding

(GO:0051015), and myosin II complex (GO:0016460) (red arrows, Fig. 4D). These results reflect the function of paclitaxel in BC-LNPs@PTX treatment. Additionally, BC-LNPs@PTX reduced the expression of proteins involved in the modification with diphosphate and geranylgeranyl owing to the inhibition of the mevalonate pathway by alendronate (blue arrows, Fig. 4D). These proteins affected the dolichyl-diphospholigosaccharide protein glycosyltransferase activity (GO:0004579), vesicle organization (GO:0016050), and endocytosis (GO:0006897). Notably, mitochondrial function was also prominently altered by BC-LNPs@PTX treatment (green arrows, Fig. 4E). Proteins related to the mitochondrial respiratory chain complex I (GO:0005747), electron carrier activity (GO:0009055), and protein import into the mitochondrial matrix (GO:0030150) were upregulated in response to the cytotoxic effects of BC-LNPs@PTX. These findings suggest that BC-LNPs@PTX regulate cellular function through the individual effects of paclitaxel and alendronate and other regulatory mechanisms, such as the mitochondria-related pathways.

We hypothesized that since mitochondria are key organelles involved in cellular metabolism[34], the disruption of mitochondrial function by BC-LNPs@PTX could change the entire process of cellular metabolism. To test this hypothesis, we first investigated the effect of BC-LNPs@PTX on glycometabolism and lipid metabolism. Using 2-NBDG, a probe for glucose uptake (Fig. 4F), we observed that BC-LNPs@PTX significantly enhanced the incorporation of glucose. Similarly, using NBD-Chol and BODIPY-C16, as lipophilic probes that separately act as the indicators of cholesterol and lipid uptake, respectively, we observed that cholesterol and lipid uptake increased after incubation with BC-LNPs@PTX (Fig. 4G−I). Therefore, proteomics analysis and these findings suggest that the tumor cells converted their metabolism to a pattern that was more dependent on exogenous glucose and lipids due to the impairment of mitochondrial functions, including the Krebs cycle. The increased requirement of glucose and lipids could be because of glycolysis and fatty acid oxidation (FAO) to compensate for the reduction in ATP levels caused by impaired mitochondrial function. Moreover, glucose and lipids might be used in the pentose phosphate pathway (PPP) to maintain redox homeostasis by reducing NADPH levels.

To test this hypothesis, we investigated the metabolites produced by 4T1 cells after BC-LNPs@PTX treatment, using the untargeted metabolomics method. All metabolites were quantified and compared with those of the negative control group (Supporting Information Fig. S11). Venn diagram analysis (Fig. 4J) elucidated that different metabolites were induced by BC-LNPs@PTX, BC-LNPs, and free paclitaxel. Notably, the alteration in metabolism caused by free paclitaxel exhibited minimum similarity with that of the BC-LNPs@PTX and BC-LNPs groups. This result was consistent with the proteomics data of the three groups as per Venn diagram analysis (Fig. 4B), elucidating the significant effect of nanoparticulated alendronate on BC-LNPs@PTX. Principal component analysis (PCA) revealed that BC-LNPs@PTX caused the most significant change in metabotypes compared with that by

analog BODIPY C16 by 4T1 cells after different treatments of 18 h detected by FCM. $n = 4$. (J) Venn diagram of the variation of metabolites in 4T1 cells after the treatment with PTX, BC-LNPs, and BC-LNPs@PTX of 24 h. (K) Principal component analysis (PCA) of metabolites detected in PTX, BC-LNPs, and BC-LNPs@PTX groups by comparing with control. $n = 5$. (L, M) KEGG analysis of the up-regulated (L) and down-regulated (M) metabolites in 4T1 cells after the treatment of BC-LNPs@PTX for 24 h by comparing with negative control. All statistical data are presented as a mean $\pm$ SEM. *$P < 0.05$; **$P < 0.01$; ***$P < 0.001$; ****$P < 0.0001$.
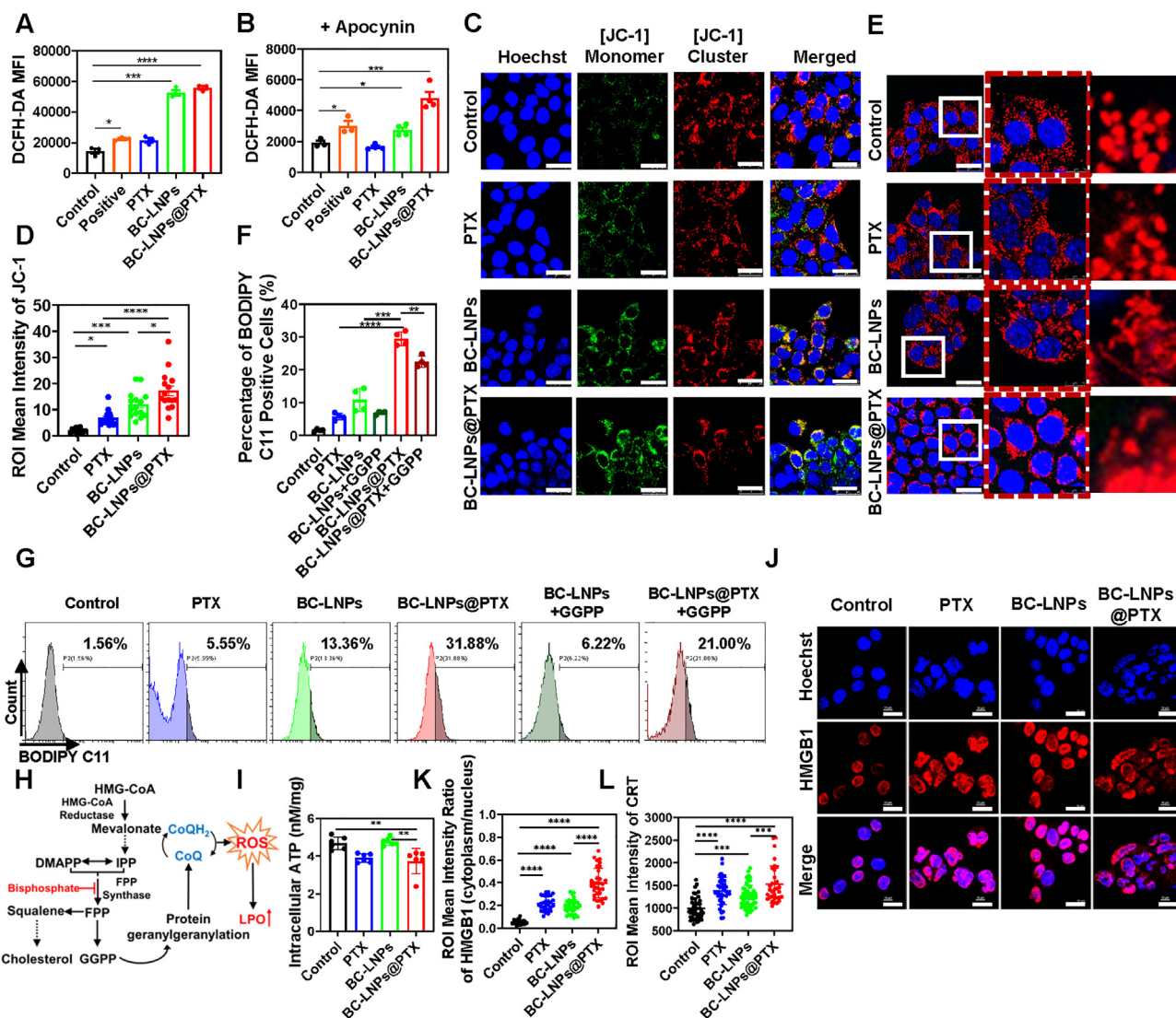
Figure 5 BC-LNPs@PTX switches the paclitaxel-induced apoptosis to the mevalonate metabolism-mediated ferroptosis. (A) The detection of total reactive oxygen species in 4T1 cells after different treatments by measuring the MFI of DCF using FCM. $n = 3$. (B) The detection of mitochondrial reactive oxygen species in 4T1 cells after different treatments plus NADPH-oxidase inhibitor (Apocynin) by measuring MFI of DCF using FCM. $n = 3$ (C, D) CLSM images (C) and the corresponding quantification (D) of mitochondrial membrane potential in 4T1 cells after different treatments based on the JC-1 staining assay. At least 15 cells were selected randomly from each group for the quantification and statistical analysis. Bar: 25 μm. (E) CLSM images of mitochondrial morphology after different treatments based on the Mtio-tracker staining. Bar: 25 μm. (F, G) The detection of lipid peroxidation levels of 4T1 cells after different treatments for 18 h by measuring MFI of BODIPY C11 using FCM. $n = 4$. (H) Mechanism diagram of bisphosphonates promoting LPO production through the inhibition of the mevalonate metabolism pathway. (I) ATP release detection of 4T1 cells after different treatments by measuring the intracellular ATP content. $n = 6$. (J, K) CLSM images (J) and the corresponding quantification (K) of HMGB1 release from the nuclear of 4T1 cells after different treatments. At least 50 cells in CLSM images were selected as the sample for the quantification. Bar: 20 μm. (L) Quantitative analysis of calreticulin release from 4T1 cells after different treatments. At least 30 cells in CLSM images were selected as the sample for the quantification. All statistical data are presented as a mean ± SEM. *$P < 0.05$; **$P < 0.01$; ***$P < 0.001$; ****$P < 0.0001$.

the BC-LNPs and free paclitaxel (Fig. 4K). This demonstrates the synergistic effect of paclitaxel and alendronate in BC-LNPs@PTX. Next, metabolite set enrichment analysis based on different annotated features was performed to explore the effect of

BC-LNPs@PTX on different metabolic pathways. As illustrated in Fig. 4L and M, BC-LNPs@PTX significantly enhanced the metabolism pathways associated with retinol, beta-alanine, and the PPP. These pathways are closely related to lipid metabolism
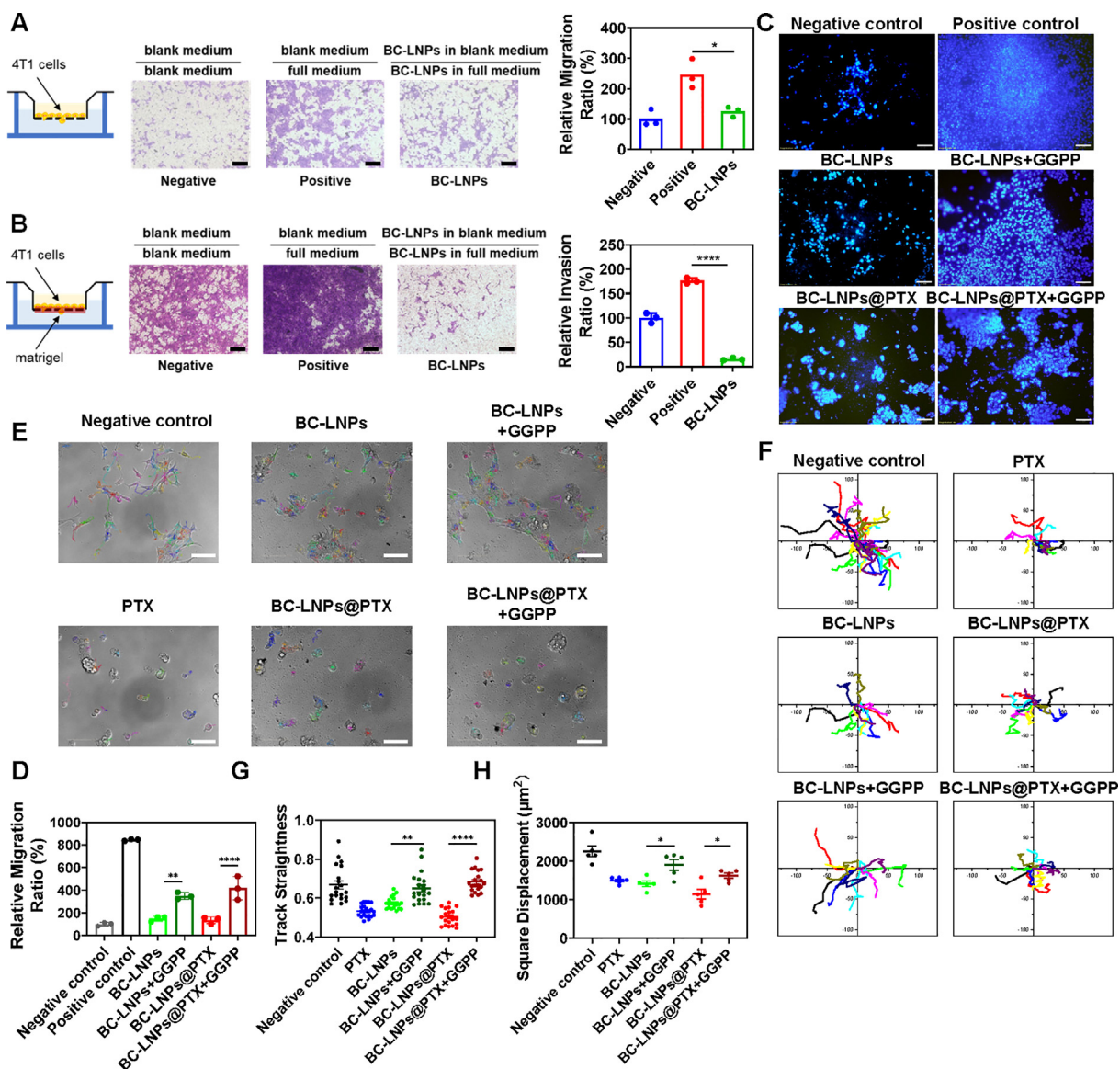
Figure 6 BC-LNPs@PTX restrains the migration and invasion of tumor cells by blocking the mevalonate metabolism pathway. (A) The migration detection of 4T1 cells by culturing cells in the upper chamber of the transwell plate and incubating with different nanogranules for 12 h. The upper and bottom chambers were added with different culture mediums. $n = 3$. Bar: 200 μm. (B) The invasion detection of 4T1 cells by culturing cells in the upper chamber of the transwell plate and incubating with different nanogranules for 12 h. The porous membrane was coated with Matrigel beforehand, and the upper and bottom chambers were added with different culture mediums. $n = 3$. Bar: 200 μm. (C) Representative microscopic images of transwell migration of 4T1 cells after different treatments. The migratory cells were labeled with Hoechst for cell counting. GGPP was used to restore the blocking of the mevalonate (MVA) pathway by alendronate. Bar: 200 μm. (D) The detection of the relative migration ratio of 4T1 cells after different treatments by comparing with the negative control group. $n = 3$. (E) The microscopic images on the real-time migration of 4T1 cells after different treatments based on the high content analysis. Bar: 100 μm. (F) The tracking trajectories of the real-time migration of 4T1 cells after different treatments based on the high content analysis. (G, H) Movement parameter detections of the real-time migration of 4T1 cells. Track straightness (G) and square displacement (H) were detected by the high content analysis technology after different treatments. At least 5 cells were selected randomly from each group for the quantification and statistic analysis. All statistical data are presented as a mean ± SEM. *$P < 0.05$; **$P < 0.01$; ***$P < 0.001$; ****$P < 0.0001$.

regulation. Retinol regulates lipid metabolism by activating the transcriptional networks controlled by retinoic acid receptors (RARs) and retinoid X receptors (RXRs)[35]. Beta-alanine is the precursor of pantothenic acid, and the latter is the core component

of CoA and acyl carrier protein (ACP)[36]. Additionally, upregulated PPP facilitates the production of reduced NADPH, which synergizes with CoA and ACP to regulate the synthesis and degradation of fatty acids[37]. Therefore, BC-LNPs@PTX treatment altered the
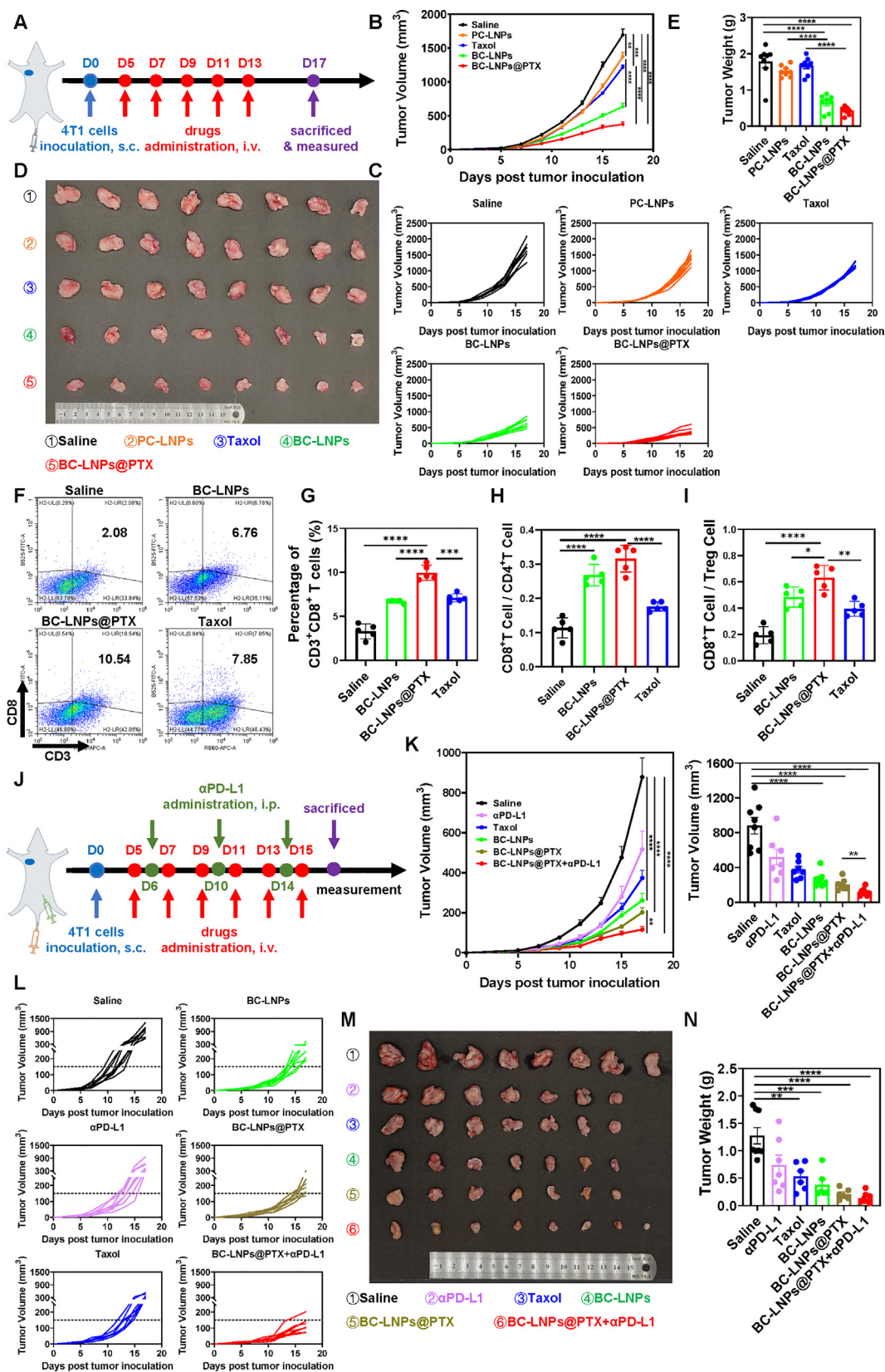
Figure 7 BC-LNPs@PTX inhibits tumor growth *in vivo* and remodels the tumor immune microenvironment to synergize with immunotherapy. (A) Schematic diagram of BC-LNPs@PTX administration in the treatment of subcutaneous 4T1 tumors. Different nanogranules and drugs were administered intravenously five times on alternate days. $n = 8$. (B, C) Growth curves of subcutaneous 4T1 tumors after the different treatments. (D, E) The anatomical imaging of tumors and tumor weight detection at day 17 after the different treatments. (F−I) The detections of tumor-infiltrating lymphocytes in subcutaneous 4T1 tumors after the above treatment strategy were analyzed by flow cytometry (FCM).

regulation of lipid metabolism by increasing the incorporation of exogenous lipids (Fig. 4G−I). Notably, these regulated metabolic pathways are also related to redox homeostasis. Retinol has antioxidant properties, and PPP increases the redox equivalent in cells. Moreover, D-arginine and cysteine metabolism were induced by BC-LNPs@PTX; they function antagonistically in ROS production[38,39]. These results indicated that tumor cells upregulated a series of pathways to maintain redox homeostasis after BC-LNPs@PTX treatment, impairing mitochondrial function. Furthermore, the disrupted mitochondrial function was verified by the alteration of metabolic pathways (Fig. 4L and M), in which cytochrome P450, nicotinate, and ubiquinone were the key mitochondrial metabolites that were affected by incubation with BC-LNPs@PTX. Therefore, these findings indicate that BC-LNPs@PTX alters mitochondrial function and redox homeostasis in tumor cells through the synergism between paclitaxel and alendronate.

3.4. BC-LNPs@PTX switches paclitaxel-induced apoptosis to mevalonate metabolism-mediated ferroptosis

Mitochondria are pivotal organelles that are involved in the regulation of cell death[40−42]; therefore, we comprehensively investigated the variation in mitochondrial function after BC-LNPs@PTX treatment to elucidate their cell death regulatory mechanism. Based on the proteomics and metabolomics data, we investigated intracellular ROS levels using DCFH-DA as the fluorescent probe. As shown in Fig. 5A, both BC-LNPs@PTX and BC-LNPs significantly induced ROS production in cells. In contrast, free paclitaxel exhibited little effect on the ROS levels. The excessive ROS is usually generated from the impaired mitochondria and from the endomembrane system where the redox homeostasis based on NADPH oxidation-reduction enzymes is disrupted. By adding extra NADPH into the medium to eliminate ROS that derived from the disordered NADPH oxidation-reduction balance, it was illustrated that BC-LNPs@PTX retained the ability to induce the production of ROS (Fig. 5B). These results suggest that the synergism between paclitaxel and alendronate in BC-LNPs@PTX markedly increased mitochondrial ROS levels.

To test the direct disruption of mitochondrial function induced by BC-LNPs@PTX, we determined the mitochondrial membrane potential ($\Delta\Psi_m$) using the JC-1 staining assay. BC-LNPs@PTX and BC-LNP treatments prominently enhanced the fluorescence signal of the JC-1 monomer, which acts as an indicator of a decrease in $\Delta\Psi_m$ (Fig. 5C and D). Free paclitaxel also moderately reduced $\Delta\Psi_m$. Notably, the decline in $\Delta\Psi_m$ further affected mitochondrial morphology. According to the CLSM images (Fig. 5E), the elliptical and dispersive morphology of the mitochondria in the control group was converted to the rod-like and cross-linked form after BC-LNPs@PTX and BC-LNP treatments. These results demonstrated that BC-LNPs@PTX directly

disturbed the function and morphology of the mitochondria, inducing mitochondrial ROS production.

The excessive production of ROS induces the accumulation of lethal LPOs, which is a unique characteristic of ferroptosis[22]. To investigate whether BC-LNPs@PTX caused ferroptosis of tumor cells by inducing excessive mitochondrial ROS production, we examined intracellular LPO levels using BODIPY-C11 as the lipid peroxide probe. As shown in Fig. 5F and G, BC-LNPs@PTX treatment led to significant LPO accumulation. Individual treatment with BC-LNPs and free paclitaxel also moderately increased the LPO content in cells. Moreover, GGPP, a key intermediate metabolite downstream of the bisphosphonate-targeted route in the mevalonate pathway[43] (Fig. 5H), partially suppressed the facilitation of LPO production by BC-LNPs@PTX. This suggests that the accumulation of LPO caused by BC-LNPs@PTX was mainly derived from the inhibition of mevalonate metabolism by alendronate.

In dying cells undergoing ferroptosis, LPO accumulation results in the rupture of the cell membrane and leakage of intracellular contents, like the process of immunogenic cell death (ICD)[44]. The released substances, including ATP, calreticulin protein (CRT), and high mobility group box 1 (HMGB1), can boost the immune response to anti-tumor therapy owing to their high immunogenicity[45]. In the present study, analysis of intracellular ATP levels revealed that BC-LNPs@PTX treatment caused ATP leakage (Fig. 5I). Additionally, BC-LNPs@PTX induced the release of HMGB1 from the nucleus and caused CRT accumulation in the cytoplasm (Fig. 5J−L, Supporting Information Fig. S12). Therefore, these findings elucidated that BC-LNPs@PTX caused ferroptosis of tumor cells more significantly by disrupting the mitochondria and inducing the accumulation of mitochondrial ROS and LPO than the apoptosis induced by paclitaxel.

3.5. BC-LNPs@PTX restrains the migration and invasion of tumor cells by blocking the mevalonate pathway

Mevalonate metabolism is not the only anabolic pathway that ends with cholesterol. The intermediate metabolites GGPP and farnesyl pyrophosphate (FPP) are widely involved in the post-translational modification of small GTPases, including RHO, RAS, and RAB family proteins, to support the anchoring of proteins in the membrane[30]. These membrane-localized small GTPases regulate vesicular transportation, membrane fusion, and cell migration through substrate conversion between GTP and GDP[29]. To explore whether BC-LNPs@PTX and BC-LNPs could suppress the migration and invasion of tumor cells, we constructed a cellular metastasis model using a transwell culture plate. Transwell membranes with and without ECM-coating were used to evaluate invasion and migration, respectively. As shown in Fig. 6A and B, 4T1 cells were inoculated in the upper chamber. The cells that moved across the pores to the back

---

Representative scatter plots (F) and percentages of CD8$^+$T cells (G) in different experimental groups were measured by FCM. Meanwhile, the ratio of CD8$^+$T cells to CD4$^+$ T cells (H) and the ratio of CD8$^+$T cells to Treg cells (I) were detected. $n = 5$. (J) Schematic diagram of BC-LNPs@PTX combined with αPD-L1 in the treatment of subcutaneous 4T1 tumors. Different nanogranules and drugs were administered intravenously six times on alternate days. αPD-L1 antibody was administered by intraperitoneal injection every 4 days, three times in total. (K, L) Tumor growth and tumor volume detection of 4T1 tumors after the different treatments. (M) Photographs of tumors on Day 17 after the different treatments. (N) Tumor weight detection at day 17 after the different treatments. Saline and BC-LNPs@PTX+αPD-L1: $n = 8$, other groups: $n = 7$. All statistical data are presented as a mean ± SEM. *$P < 0.05$; **$P < 0.01$; ***$P < 0.001$; ****$P < 0.0001$.
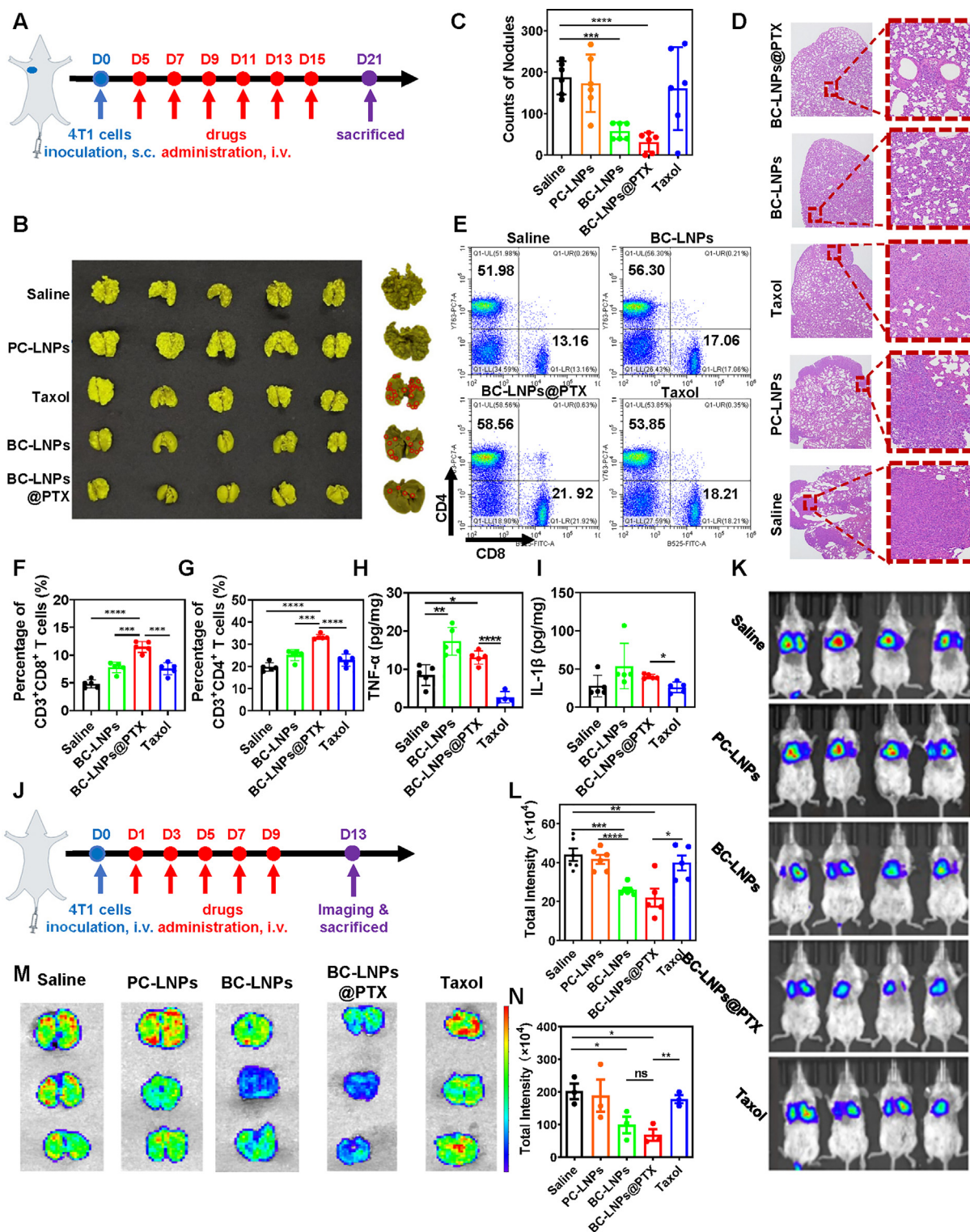
Figure 8   BC-LNPs@PTX inhibits the tumor BC-LNPs@PTX suppresses the tumor metastasis *in vivo* by inhibiting the mevalonate metabolism pathway. (A) Schematic diagram of BC-LNPs@PTX administration in the treatment of spontaneous lung metastasis from subcutaneous 4T1 tumors. (B, C) Photographs (B) and the corresponding quantification (C) of metastatic nodules in the lung after different treatments. $n = 6$. The red circles represented the metastatic nodules in the lung. (D) H&E staining images of lung metastatic nodules after different treatments. Magnification: 200×. (E−G) The detections of splenic lymphocytes after the above treatment strategy were analyzed by flow cytometry (FCM). Representative scatter plots (E), percentages of CD8+T cells (F) and CD4+ T cells (G) in different experimental groups were measured by FCM. $n = 5$. (H, I) Serum proinflammatory cytokine detections of TNF-α (H) and IL-1β (I) in different experimental groups measured by ELISA. (J) Schematic diagram of BC-LNPs@PTX administration in the treatment of induced lung metastasis by intravenous injection of 4T1-luc cells, $n = 6$. (K, L) IVIS images (K) and the corresponding fluorescence intensity detection (L) of tumor-bearing mice after different treatments. (M, N) IVIS images (M) and the corresponding fluorescence intensity detection (N) of the lungs after sacrifice and dissection after the different treatments. All statistical data are presented as a mean ± SEM. *$P < 0.05$; **$P < 0.01$; ***$P < 0.001$; ****$P < 0.0001$.

of the transwell membrane were stained and quantified. Compared to the control group, BC-LNPs significantly reduced the migration and invasion of cells. Cell counting analysis also demonstrated the same results (Fig. 6C and D). Moreover, GGPP supplementation during BC-LNPs@PTX and BC-LNP treatments restored the migration capacity of the tumor cells. This suggests that BC-LNPs inhibited the migration and invasion of tumor cells by suppressing the mevalonate pathway. In addition, cell migration dynamics analysis (Fig. 6E, Supporting Information Movies S1−S6) revealed that BC-LNPs@PTX, BC-LNPs, and free paclitaxel treatments limited cellular motion and decreased the movement range of cells (Fig. 6F). The quantification of multiple pavement parameters, including displacement, track straightness speed, and accumulated distance, demonstrated their inhibitory efficacy (Fig. 6G and H, Supporting Information Fig. S13). Notably, the GGPP addition recovered the cellular motion to some extent. Therefore, these findings confirmed the ability of BC-LNPs@PTX to inhibit cell migration and invasion by limiting the motion range and speed of cells in a mevalonate metabolism-dependent manner.

Supplementary video related to this article can be found at https://doi.org/10.1016/j.apsb.2023.08.029

3.6. BC-LNPs@PTX inhibits tumor growth in vivo and remodels the tumor immune microenvironment to synergize with immunotherapy

Next, we investigated the efficacy of BC-LNPs@PTX *in vivo* using a 4T1 tumor-bearing mouse model. Tumor-targeting ability was first evaluated using the *in vivo* living imaging system (IVIS). We used the fluorescent lipid probe DIR, as an *in vivo* indicator, for this experiment, which revealed that BC-LNPs were quickly delivered to the tumor tissue after 1 h of intravenous injection and were accumulated in high concentrations in the tumor for up to 72 h (Supporting Information Fig. S14). The analyses of pharmacokinetics and biodistribution further showed that BC-LNPs@PTX treatment caused greater peak concentration (C_{max}) but faster elimination compared to Taxol (Supporting Information Figs. S15 and S16). These findings suggested more drugs in BC-LNPs@PTX could be rapidly delivered to the tumor in the early phase after administration and be stranded to take a long-time effect. After that, the *in vivo* antitumor efficacy of BC-LNPs@PTX was investigated according to the protocol presented in Fig. 7A. PC-LNPs and the classical paclitaxel preparation Taxol were used as controls. As shown in Fig. 7B and C, BC-LNPs@PTX exhibited the highest efficacy after five administrations. BC-LNPs and Taxol exerted moderate therapeutic effects. The anatomical imaging in Fig. 7D and E further demonstrated the most significant tumor suppression effect after BC-LNPs@PTX treatment, as evidenced by the smallest tumors and lightest tumor weight, which also had no negative effect on the body weight and hematological indices of mice (Supporting Information Fig. S17). Next, to further confirm the *in vivo* therapeutical effect of BC-LNPs@PTX, we constructed the orthotopic breast cancer model by directly injecting 4T1 breast cancer cells into the fat pad of the fourth pair of mammary glands on the right side of mice (Supporting Information Fig. S18). The proliferation of orthotopic breast tumors was directly observed and measured by vernier caliper. Notably,

BC-LNPs@PTX also exhibited the highest efficacy. These findings showed high consistency with the results from the subcutaneous tumor-bearing model, highlighting the synergism between PTX and alendronate *in vivo* cancer therapy and exhibiting the significance of nanoparticle construction.

To determine the synergistic mechanism, we explored the tumor immune microenvironment after treatment. The lymphatic subset analysis based on FCM elucidated that BC-LNPs@PTX significantly induced an increase in CD8+ T lymphocytes and a reduction in immunosuppressive Treg cells in tumors compared to that in the BC-LNPs and Taxol groups (Fig. 7F and G, Supporting Information Fig. S19). Correspondingly, BC-LNPs@PTX treatment significantly increased the ratios of CD8+/CD4+ T cells and CD8+/Treg cells (Fig. 7H and I). In addition, we examined the activation of DCs in tumor-draining lymph nodes (TDLNs) and showed that BC-LNPs@PTX induced the maximum degree of DCs maturation, while BC-LNPs and Taxol had comparable effects (Supporting Information Fig. S20). This suggests that BC-LNPs@PTX remodeled the tumor immune microenvironment by enhancing the cytotoxic immune response and attenuating suppressive immunity[46]. Notably, nanoparticulated alendronate was more responsible for this remodeling capacity because BC-LNPs, but not Taxol, exhibited an immunopotentiation effect to some extent[33]. This indicated that mevalonate metabolism-mediated ferroptosis mainly triggered the enhancement of the immune response.

Previous studies have reported that ferroptosis, because of its immunopotentiation effect, has great synergistic potential with immunotherapy[47]. To test the synergistic effect of ferroptosis and BC-LNPs@PTX, we first investigated the effect of BC-LNPs@PTX on the expression of immunosuppressive receptor PD-L1 in cancer cells. Strikingly, BC-LNPs@PTX treatment significantly increased the expression of PD-L1 in 4T1 cells (Supporting Information Fig. S21). It meant the cancer cells treated by BC-LNPs@PTX might be more sensitive to the therapy based on immune checkpoint blocker αPD-L1. To test that, the *in vivo* effect of BC-LNPs@PTX combined with αPD-L1 was investigated according to the protocol in Fig. 7J. A single treatment with αPD-L1 exhibited a weak effect owing to the suppressive immune microenvironment in 4T1 tumors. However, the combination of BC-LNPs@PTX and αPD-L1 markedly enhanced therapeutic efficacy, especially when compared to that of BC-LNPs@PTX alone (Fig. 7K−N), indicating the sensitization effect of BC-LNPs@PTX on the αPD-L1 therapy. These findings suggest that BC-LNPs@PTX effectively synergizes with immunotherapy by inducing ferroptosis in cancer cells and remodeling the tumor immune microenvironment.

3.7. BC-LNPs@PTX suppresses tumor metastasis in vivo by inhibiting the mevalonate pathway

The inhibitory effect of BC-LNPs@PTX on tumor metastasis was investigated by constructing spontaneous and induced metastasis models. According to the methodology presented in Fig. 8A, the mice were subcutaneously inoculated with 4T1 cells and fed to induce spontaneous pulmonary metastasis. The mice were sacrificed after six doses of administration, and the lungs were extracted to detect metastatic lesions. Photographs of the lungs after the different treatments revealed that pulmonary metastasis was markedly suppressed by BC-LNPs@PTX (Fig. 8B). Quantification based on metastasis nodule counting revealed that BC-

LNPs@PTX had the greatest inhibitory efficacy (Fig. 8C). Notably, BC-LNPs also significantly inhibited pulmonary metastasis, whereas Taxol exhibited no inhibitory effect. The histological analysis revealed that BC-LNPs@PTX treatment effectively restored the morphology of the pulmonary alveoli, demonstrating the highest efficacy (Fig. 8D).

Next, to explore the underlying mechanism, we investigated the systemic immune response after different treatments. We observed that BC-LNPs@PTX significantly increased CD8$^+$ and CD4$^+$ T lymphocytes in the spleen (Fig. 8E−G). The ratios of CD8$^+$/CD4$^+$ T cells and CD8$^+$/Treg cells were also significantly increased by BC-LNPs@PTX treatment (Supporting Information Fig. S22). Additionally, both BC-LNPs@PTX and BC-LNPs markedly increased serum TNF-α and IL-1β concentration, but Taxol treatment exhibited the same effects as that of the control (Fig. 8H and I). Meanwhile, enhanced immunity had no effect on body weight, organ structure, and multiple hematological indices, indicating the safety of the treatment (Supporting Information Figs. S23 and S24).

Finally, we developed a short-term induced metastasis model by intravenously injecting 4T1-luc cells in the mice to promote tumor metastasis to the lungs (Fig. 8J). The results revealed that fewer cancer cells colonized the lungs after BC-LNPs@PTX treatment (Fig. 8K and L). Amplified images of the lungs after sacrifice and dissection further confirmed the inhibitory efficacy of BC-LNPs@PTX and BC-LNPs (Fig. 8M and N). Histological analysis confirmed these results (Supporting Information Fig. S25). Moreover, BC-LNPs@PTX were safe after the therapy of the induced metastasis model (Supporting Information Figs. S26 and S27). Therefore, these findings suggest that BC-LNPs@PTX suppressed tumor metastasis *in vivo* by enhancing the systemic immune response. Moreover, it demonstrates that the systematic immunopotentiation effect was primarily derived from the inhibition of the mevalonate pathway.

4. Conclusions

In the present study, we designed and fabricated BC-LNPs@PTX to achieve co-delivery of alendronate and paclitaxel to target tumor tissue. BC-LNPs@PTX contained a "core−shell" structure, where alendronate coordinated with calcium ions to form the solid core, and a lipid layer containing paclitaxel was coated to form the shell. This structural feature guaranteed that alendronate could be effectively delivered to the tumor and released in the acidic endosomal environment, avoiding the natural tropism of bisphosphonate drugs to the bone. Alendronate significantly enhanced the tumor-killing effect of paclitaxel and altered its cytotoxic mechanism (Fig. 1), thus exhibiting synergy. In contrast to paclitaxel-induced apoptosis, nanoparticulated alendronate changed the morphology and function of mitochondria, induced metabolism based on exogenous glucose and lipids, and disturbed redox homeostasis in tumor cells. Therefore, BC-LNPs@PTX induced the production of excessive amounts of ROS in the mitochondria, leading to the accumulation of lethal LPO and triggering ferroptosis characterized by the leakage of intracellular substances. Moreover, since the inhibition of the mevalonate pathway by alendronate blocked the posttranslational modification of small GTPases related to cell migration, BC-LNPs@PTX prominently suppressed tumor metastasis by limiting the motion range and speed of cancer cells and enhancing the systematic immunopotentiation effect. Thus, the co-delivery of alendronate and paclitaxel markedly enhanced the anti-tumor synergism of

chemotherapy and immunotherapy by switching paclitaxel-induced apoptosis to mevalonate metabolism-mediated ferroptosis. This highlights the potential of tumor metabolism regulation in cancer therapy and provides new insights for the development of cytotoxic drugs in combination with metabolic regulators.

Author contributions

Ge Song: Conceptualization, Methodology, Validation, Investigation, Data Curation, Writing - Original Draft, Visualization. Minghui Li: Conceptualization, Methodology, Validation, Investigation, Data Curation, Writing - Original Draft, Visualization. Shumin Fan: Conceptualization, Methodology, Validation, Investigation, Data Curation, Writing - Original Draft, Visualization. Mengmeng Qin: Investigation. Bin Shao: Resources, Supervision. Wenbing Dai: Resources, Supervision, Funding acquisition. Hua Zhang: Resources, Supervision. Xueqing Wang: Resources, Supervision, Funding acquisition. Bing He: Conceptualization, Writing - review & editing, Supervision, Project administration, Funding acquisition. Qiang Zhang: Conceptualization, Writing - review & editing, Supervision, Project administration, Funding acquisition.

Conflicts of interest

The authors declare no conflict of interest.

Appendix A.   Supporting information

Supporting data to this article can be found online at https://doi.org/10.1016/j.apsb.2023.08.029.

References

1. Savage P, Stebbing J, Bower M, Crook T. Why does cytotoxic chemotherapy cure only some cancers?. *Nat Clin Pract Oncol* 2009;**6**: 43−52.
2. Galluzzi L, Buque A, Kepp O, Zitvogel L, Kroemer G. Immunological effects of conventional chemotherapy and targeted anticancer agents. *Cancer Cell* 2015;**28**:690−714.
3. Fennell DA, Summers Y, Cadranel J, Benepal T, Christoph DC, Lal R, et al. Cisplatin in the modern era: the backbone of first-line chemotherapy for non-small cell lung cancer. *Cancer Treat Rev* 2016;**44**: 42−50.
4. Niu Q, Liu Y, Zheng Y, Tang Z, Qian Y, Qi R, et al. Co-delivery of nigericin and decitabine using hexahistidine-metal nanocarriers for pyroptosis-induced immunotherapeutics. *Acta Pharm Sin B* 2022;**12**: 4458−71.
5. DeSantis CE, Lin CC, Mariotto AB, Siegel RL, Stein KD, Kramer JL, et al. Cancer treatment and survivorship statistics. 2014 *CA Cancer J Clin* 2014;**64**:252−71.
6. Gambacorti-Passerini C, Kantarjian HM, Kim DW, Khoury HJ, Turkina AG, Brummendorf TH, et al. Long-term efficacy and safety of bosutinib in patients with advanced leukemia following

resistance/intolerance to imatinib and other tyrosine kinase inhibitors. *Am J Hematol* 2015;**90**:755−68.

7. Lesokhin AM, Callahan MK, Postow MA, Wolchok JD. On being less tolerant: enhanced cancer immunosurveillance enabled by targeting checkpoints and agonists of T cell activation. *Sci Transl Med* 2015;**7**:280sr1.

8. Galluzzi L, Vitale I, Warren S, Adjemian S, Agostinis P, Martinez AB, et al. Consensus guidelines for the definition, detection, and interpretation of immunogenic cell death. *J Immunother Canc* 2020;**8**: e000337.

9. D'Eliseo D, Manzi L, Velotti F. Capsaicin as an inducer of damage-associated molecular patterns (DAMPs) of immunogenic cell death (ICD) in human bladder cancer cells. *Cell Stress Chaperones* 2013;**18**: 801−8.

10. Galluzzi L, Senovilla L, Zitvogel L, Kroemer G. The secret ally: immunostimulation by anticancer drugs. *Nat Rev Drug Discov* 2012; **11**:215−33.

11. Liu L, Mayes PA, Eastman S, Shi H, Yadavilli S, Zhang TD, et al. The BRAF and MEK inhibitors dabrafenib and trametinib: effects on immune function and in combination with immunomodulatory antibodies targeting PD-1, PD-L1, and CTLA-4. *Clin Cancer Res* 2015; **21**:1639−51.

12. Vacchelli E, Galluzzi L, Fridman WH, Galon J, Sautes-Fridman C, Tartour E, et al. Trial watch chemotherapy with immunogenic cell death inducers. *OncoImmunology* 2012;**1**:179−88.

13. Johnstone RW, Ruefli AA, Lowe SW. Apoptosis: a link between cancer genetics and chemotherapy. *Cell* 2002;**108**:153−64.

14. Wallach D, Kang TB, Dillon CP, Green DR. Programmed necrosis in inflammation: toward identification of the effector molecules. *Science* 2016;**352**:aaf2154.

15. Banstola A, Poudel K, Kim JO, Jeong JH, Yook S. Recent progress in stimuli-responsive nanosystems for inducing immunogenic cell death. *J Control Release* 2021;**337**:505−20.

16. Ngwa W, Irabor OC, Schoenfeld JD, Hesser J, Demaria S, Formenti SC. Using immunotherapy to boost the abscopal effect. *Nat Rev Cancer* 2018;**18**:313−22.

17. Kepp O, Marabelle A, Zitvogel L, Kroemer G. Oncolysis without viruses—inducing systemic anticancer immune responses with local therapies. *Nat Rev Clin Oncol* 2020;**17**:49−64.

18. Kroemer G, Galassi C, Zitvogel L, Galluzzi L. Immunogenic cell stress and death. *Nat Immunol* 2022;**23**:487−500.

19. Jiang X, Stockwell BR, Conrad M. Ferroptosis: mechanisms, biology and role in disease. *Nat Rev Mol Cell Biol* 2021;**22**:266−82.

20. Dixon SJ, Lemberg KM, Lamprecht MR, Skouta R, Zaitsev EM, Gleason CE, et al. Ferroptosis: an iron-dependent form of non-apoptotic cell death. *Cell* 2012;**149**:1060−72.

21. Lei G, Zhuang L, Gan B. Targeting ferroptosis as a vulnerability in cancer. *Nat Rev Cancer* 2022;**22**:381−96.

22. Li D, Li Y. The interaction between ferroptosis and lipid metabolism in cancer. *Signal Transduct Target Ther* 2020;**5**:108.

23. Masaldan S, Bush AI, Devos D, Rolland AS, Moreau C. Striking while the iron is hot: iron metabolism and ferroptosis in neurodegeneration. *Free Radical Biol Med* 2019;**133**:221−33.

24. Gan B. Mitochondrial regulation of ferroptosis. *J Cell Biol* 2021 :220:e202105043.

25. Zhu S, Zhang QH, Sun XF, Zeh HJ, Lotze MT, Kang R, et al. HSPA5 regulates ferroptotic cell death in cancer cells. *Cancer Res* 2017;**77**: 2064−77.

26. Bersuker K, Hendricks JM, Li Z, Magtanong L, Ford B, Tang PH, et al. The CoQ oxidoreductase FSP1 acts parallel to GPX4 to inhibit ferroptosis. *Nature* 2019;**575**:688−92.

27. Doll S, Freitas FP, Shah R, Aldrovandi M, da Silva MC, Ingold I, et al. FSP1 is a glutathione-independent ferroptosis suppressor. *Nature* 2019;**575**:693−8.

28. Zheng J, Conrad M. The metabolic underpinnings of ferroptosis. *Cell Metabol* 2020;**32**:920−37.

29. Juarez D, Fruman DA. Targeting the mevalonate pathway in cancer. *Trends Cancer* 2021;**7**:525−40.

30. Mullen PJ, Yu R, Longo J, Archer MC, Penn LZ. The interplay between cell signalling and the mevalonate pathway in cancer. *Nat Rev Cancer* 2016;**16**:718−31.

31. Garwood ER, Kumar AS, Baehner FL, Moore DH, Au A, Hylton N, et al. Fluvastatin reduces proliferation and increases apoptosis in women with high grade breast cancer. *Breast Cancer Res Treat* 2010; **119**:137−44.

32. Li M, Qin M, Song G, Deng H, Wang D, Wang X, et al. A biomimetic antitumor nanovaccine based on biocompatible calcium pyrophosphate and tumor cell membrane antigens. *Asian J Pharm Sci* 2021;**16**: 97−109.

33. Qin M, Li M, Song G, Yang C, Wu P, Dai W, et al. Boosting innate and adaptive antitumor immunity *via* a biocompatible and carrier-free nanovaccine engineered by the bisphosphonates-metal coordination. *Nano Today* 2021;**37**:101097.

34. Mills EL, Kelly B, O'Neill LAJ. Mitochondria are the powerhouses of immunity. *Nat Immunol* 2017;**18**:488−98.

35. Pang XY, Wang S, Jurczak MJ, Shulman GI, Moise AR. Retinol saturase modulates lipid metabolism and the production of reactive oxygen species. *Arch Biochem Biophys* 2017;**633**:93−102.

36. Jackowski S, Rock CO. Regulation of coenzyme a biosynthesis. *J Bacteriol* 1981;**148**:926−32.

37. Patra KC, Hay N. The pentose phosphate pathway and cancer. *Trends Biochem Sci* 2014;**39**:347−54.

38. Mandal PK, Seiler A, Perisic T, Kölle P, Banjac Canak A, Förster H, et al. System x(c)⁻ and thioredoxin reductase 1 cooperatively rescue glutathione deficiency. *J Biol Chem* 2010;**285**:22244−53.

39. Wang S, Li F, Qiao R, Hu X, Liao H, Chen L, et al. Arginine-rich manganese silicate nanobubbles as a ferroptosis-inducing agent for tumor-targeted theranostics. *ACS Nano* 2018;**12**:12380−92.

40. Zhou R, Yazdi AS, Menu P, Tschopp J. A role for mitochondria in NLRP3 inflammasome activation. *Nature* 2011;**469**:221−5.

41. Shimada K, Crother TR, Karlin J, Dagvadorj J, Chiba N, Chen S, et al. Oxidized mitochondrial DNA activates the NLRP3 inflammasome during apoptosis. *Immunity* 2012;**36**:401−14.

42. Nakahira K, Haspel JA, Rathinam VA, Lee SJ, Dolinay T, Lam HC, et al. Autophagy proteins regulate innate immune responses by inhibiting the release of mitochondrial DNA mediated by the NALP3 inflammasome. *Nat Immunol* 2011;**12**:222−30.

43. Wiemer AJ, Wiemer DF, Hohl RJ. Geranylgeranyl diphosphate synthase: an emerging therapeutic target. *Clin Pharmacol Ther* 2011;**90**:804−12.

44. Dang Q, Sun Z, Wang Y, Wang L, Liu Z, Ferroptosis Han X. Ferroptosis: a double-edged sword mediating immune tolerance of cancer. *Cell Death Dis* 2022;**13**:925.

45. Efimova I, Catanzaro E, Van der Meeren L, Turubanova VD, Hammad H, Mishchenko TA, et al. Vaccination with early ferroptotic cancer cells induces efficient antitumor immunity. *J Immunother Cancer* 2020;**8**:e001369.

46. Xu Y, Xiong J, Sun X, Gao H. Targeted nanomedicines remodeling immunosuppressive tumor microenvironment for enhanced cancer immunotherapy. *Acta Pharm Sin B* 2022;**12**:4327−47.

47. Friedmann Angeli JP, Krysko DV, Conrad M. Ferroptosis at the crossroads of cancer-acquired drug resistance and immune evasion. *Nat Rev Cancer* 2019;**19**:405−14.